Open Access

Recent Progress in Materials

LIDSEN Publishing Inc.

Original Research

Assessing the Limitations of DFT and TD-DFT Calculations for Spectroscopic and Electrochemical Properties of Azo-Amino Acid Schiff Base Cu(II) Complexes

Ayumu Hirayama [1], Mao Narita [1], Shota Ito [1], Daisuke Nakane [1], Shimaa Hosny [2], Takashiro Akitsu [1,*]

1. Department of Chemistry, Faculty of Science, Tokyo University of Science, 1-3 Kagurazaka, Shinjuku-ku, Tokyo 162-8601, Japan; E-Mails: 1326612@ed.tus.ac.jp; 2026603@ed.tus.ac.jp; 1324517@ed.tus.ac.jp; a29776@rs.tus.ac.jp; akitsu2@rs.tus.ac.jp
2. Department of Chemistry, Faculty of Science, New Valley University, Alkharga 72511, Egypt; E-Mail: shimaahosny@sci.nvu.edu.eg

* **Correspondence:** Takashiro Akitsu; E-Mail: akitsu2@rs.tus.ac.jp

Academic Editor: Qudong Wang

Special Issue: Research on Hybrid Materials of Metal Complexes

Recent Progress in Materials
2026, volume 8, issue 3
doi:10.21926/rpm.2603008

Received: June 30, 2026
Accepted: September 08, 2026
Published: September 13, 2026

Abstract

In this study, we assessed the reliability and limitations of density functional theory (DFT) and time-dependent density functional theory (TD-DFT) in predicting the spectroscopic and electrochemical properties of four azo-amino acid Schiff-base Cu(II) complexes by comparing calculated ultraviolet-visible (UV-vis) absorption and circular dichroism (CD) spectra and reduction potentials with experimental data obtained from spectroscopic measurements and cyclic voltammetry (CV). The optimized coordination geometries were generally close to square planar, whereas the phenylalanine complex showed the largest distortion, with a τ_4 value of 0.204. TD-DFT reproduced some major features of the experimental UV-vis and CD spectra qualitatively; however, the calculated UV-vis bands were generally shifted toward shorter wavelengths, whereas the CD spectra showed discrepancies in wavelength, intensity, and sign. In particular, the positive experimental CD features in the approximately 300-325

nm region were predicted with the opposite sign for all four complexes. For the Cu(II)/Cu(I) couples, the calculated reduction potentials differed by 0.21-0.32 V between the two computational protocols, and the predicted ordering of reducibility also changed between the two protocols. Moreover, this ordering was inconsistent with the trend inferred from the lowest unoccupied molecular orbital energies. These results demonstrate that agreement in spectral peak positions or frontier-orbital trends alone is insufficient to establish the quantitative reliability of DFT and TD-DFT predictions for transition-metal complexes. Property-specific benchmarking and careful treatment of structural relaxation, solvation, and possible conformational variability are therefore required when applying these methods to such systems in solution.

Keywords
Azo-amino acid Schiff base Cu(II) complexes; DFT calculations; TD-DFT calculations; UV-vis spectra; circular dichroism spectra; reduction potential; implicit solvation model

1. Introduction

Density functional theory (DFT) calculations of the physical properties of transition metal complexes can predict properties by carefully selecting computational parameters such as the functional and basis set. DFT, developed by Kohn and Sham, is a non-parametric quantum mechanical method that enables a more detailed and quantitative description of electronic structures and energy levels [1, 2]. This has made it possible to calculate the magnetic and spectroscopic properties, molecular structure, and electronic structure of metal complexes, and DFT has been used for many yearsto study transition metal complexes [2]. Furthermore, in recent years, the adoption of gradient-corrected and hybrid functionals has improved the agreement between computational and experimental results. Time-dependent density functional theory (TD-DFT) enables the calculation of excitation energies and optical absorption spectra by investigating changes in electron density under time-dependent conditions and is used to study electronic excitation [2, 3].

However, its accuracy varies greatly depending on the physical property of interest and the system; while it is relatively reliable for reaction energies and structural optimization, it has been pointed out that quantities such as the gap between the highest occupied molecular orbital (HOMO) and the lowest unoccupied molecular orbital (LUMO), spin states, and redox potentials are highly dependent on the calculation conditions and the treatment of the environment [4]. In transition metal complexes in particular, spin multiplet competition and closely spaced electronic states often arise because the electronic configuration changes due to slight variations in the d-orbital occupancy of the metal center, the ligand field, or the coordination geometry [5, 6]. One computational factor contributing to this dependence is the self-interaction error inherent in DFT calculations and the resulting excessive charge delocalization [7, 8]. These effects systematically influence orbital ordering, energy gaps, and charge transfer. Therefore, even when an empirical correlation is observed between frontier orbital levels and redox susceptibility [9], orbital energies alone have limited utility for quantitatively estimating redox potentials in solution [10].

A similar trend is observed in TD-DFT calculations: while local excitations, such as π-π* transitions within ligands, are relatively easy to reproduce, excitation energies may systematically deviate in excited states involving metal-to-ligand charge transfer, ligand-to-metal charge transfer or charge transfer between ligands. In particular, for long-range charge-transfer transitions, commonly used exchange-correlation approximations in TD-DFT may underestimate excitation energies [11, 12]. This limitation is related to the asymptotic behavior of exchange-correlation potentials and self-interaction error, which can cause systematic errors in transitions with large charge-transfer components [11, 12]. Furthermore, while circular dichroism (CD) spectra are also important in systems containing chiral elements, it is not easy to sufficiently reproduce the experimental shapes and relative intensities using excitation calculations based on a single structure alone, as these spectra are sensitive to minute structural differences and the surrounding environment, such as the solvent [13].

Treating solvent effects is critical in calculating spectroscopic and electrochemical properties. Since electronic states are strongly influenced by stabilization through solvation [14-17], several solvation models have been developed to incorporate this effect into calculations. One such model, the implicit solvation model, treats the solvent as a continuous polar medium-that is, as a mean field-significantly reducing computational cost while allowing the solvent environment to be incorporated [14-17]. However, since this model cannot directly represent specific interactions such as the local orientation of solvent molecules, ion-pair formation, and hydrogen bonding, errors become apparent when reproducing excited states or redox potentials where the charge distribution changes significantly [14-17]. Explicit solvation models, which incorporate individual solvent molecules into the calculation, also exist and can describe electrostatic and non-covalent interactions more directly [14, 18]. On the other hand, since the size of the computational system increases, this approach involves increased computational complexity and longer calculation times, making it difficult to apply to large systems. Furthermore, calculating redox potentials by evaluating Gibbs free-energy differences (ΔG) by including structural relaxation, thermal corrections, and solvation free energy constitutes a theoretically framework [19-21]. The computational framework for predicting redox potentials in solution, including the treatment of reference electrodes, has been systematically developed, allowing calculations under conditions closer to those observed experimentally [21, 22]. However, the predicted values depend heavily on the choice of functional, basis set, and solvation model.

Recent studies have increasingly integrated experimental characterization with computational analyses of Schiff-base and amino-acid-containing metal complexes, including Cu(I) and Cu(II) systems, to investigate their molecular structures, electronic properties, and molecular interactions [23-25]. DFT- and TD-DFT-based excited-state analyses have also been applied to conjugated chromophores to examine their absorption and charge-transfer characteristics [26]. These studies illustrate the broad utility of computational approaches, while the predictive performance of a given computational protocol must still be assessed separately for each target property. Against this background, it is significant to compare observables, such as those from spectroscopy and electrochemistry, from the perspective of the limitations of density functional approximations and solvation and environment models, to clarify where and under what conditions assumptions are likely to break down. In this study, we aim to assess the limitations of DFT calculations for transition metal complexes in solution by comparing experimental data from ultraviolet-visible (UV-vis) absorption and CD spectroscopy and cyclic voltammetry (CV) with various parameters obtained

from DFT and TD-DFT calculations for four azo-amino acid Schiff-base Cu(II) complexes containing substituents derived from different amino acids. Here, the main point is not simply to compare calculated and experimental data, but to see where the calculations begin to deviate from the real measurements. The discussion therefore focuses on how small changes in coordination geometry, solvent treatment, and computational protocol can influence the predicted spectra and redox behavior of these Cu(II) complexes. Regarding solvent effects, we used the solvation model based on density (SMD), an implicit solvation model, prioritizing computational efficiency and ease of use, and discussed its limitations. Furthermore, to assess the dependence of ΔG-based redox-potential predictions on the overall computational protocol, we compared the conventional B3LYP functional [27, 28] combined with the 6-31+G(d) basis set for light atoms [29] and LANL2DZ for Cu [30] with a wB97X-D-based protocol [31] using def2-TZVP for geometry optimization and vibrational frequency calculations and def2-TZVPP for the final single-point energy calculations [32].

The four Cu(II) complexes examined in this study were also considered as candidate redox mediators for laccase-based bioelectrochemical systems. Laccase is a multicopper oxidase that accepts electrons from organic substrates or metal ions and catalyzes the four-electron reduction of oxygen to water [33]. This protein is used on the cathode side of biofuel cells; however, the power conversion efficiency of such systems can be limited, and a mediator, such as a metal complex, can be introduced between the protein and the electrode to facilitate electron transfer [34]. In this context, reliable computational prediction of redox energetics and spectroscopic properties is important for relating molecular structure to experimentally observable behavior and for evaluating the suitability of such complexes as redox mediators. Assessing the limitations of DFT and TD-DFT is therefore important for identifying which calculated trends can be interpreted reliably and where method- or environment-dependent errors may affect conclusions regarding the behavior of these complexes in solution. Accordingly, docking calculations with laccase were performed to examine the possible influence of the local protein environment on each complex. The resulting docking poses were used as qualitative models of the molecular environment surrounding the complexes.

2. Materials and Methods

2.1 Experimental Methods

The four complexes investigated in this study were previously reported azo-amino acid Schiff base Cu(II) complexes containing substituents derived from arginine, phenylalanine, threonine, and valine (the R groups in Figure 1), hereafter abbreviated as the Arg, Phe, Thr, and Val complexes, respectively [35, 36]. We previously described the synthesis and characterization of these complexes [36], and we prepared the complexes used in the present study according to the reported procedure.

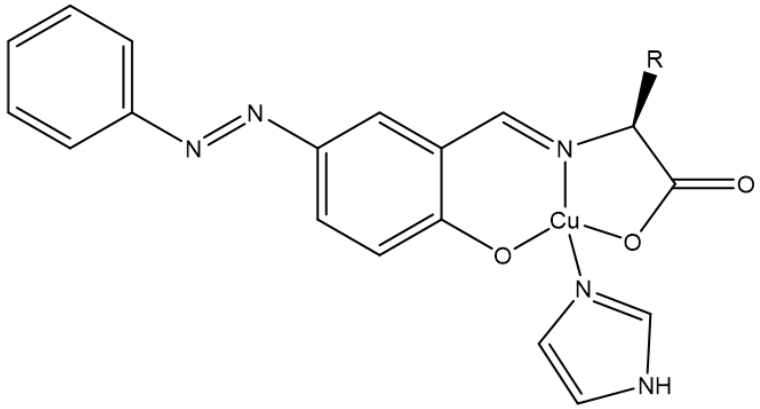

Figure 1 Structures of azo-amino acid Schiff base Cu(II) Complexes (R: $-(CH_2)_3-NH-C(=NH)-NH_2$ (Arg complex), $-CH_2-C_6H_5$ (Phe complex), $-CH(OH)-CH_3$ (Thr complex), $-CH(CH_3)_2$ (Val complex)).

2.2 Physical Measurements

UV-vis spectra were measured using a JASCO V-650 spectrophotometer at 298 K as methanol solutions in a 10 mm pathlength cell over the range of 200-600 nm. CD spectra were measured using a JASCO J-820 spectropolarimeter under the same conditions as the UV-vis measurements (298 K, methanol) in a 10 mm pathlength cell over the range of 200-600 nm. CV measurements were performed using a BAS SEC2000-UV-vis and an ALS2323 BI-POTENTIOSTAT. A glassy carbon electrode was used as the working electrode, a platinum wire as the counter electrode, and an Ag/AgCl electrode as the reference electrode. Measurements were conducted in phosphate buffer adjusted to pH 7. We used ultrapure water only to prepare the electrode-modification suspensions; we did not use it as the electrolyte medium for the CV measurements. The scan rate was 0.05 V/s, and the potential range was -1.0 to +1.0 V vs Ag/AgCl. For comparison with the calculated potentials, the potentials measured versus Ag/AgCl were approximately converted to the SHE scale by applying an offset of +0.20 V.

2.3 Computational Methods

DFT and TD-DFT calculations were performed using Gaussian 09, Revision E.01 [37] for the physical properties of four azo-amino acid Schiff base Cu(II) complexes. We used GaussView 5 to build the molecular structures and visualize the results. Solvent effects were considered using the SMD implicit solvation model [17], with the solvent specified according to each experimental condition.

2.3.1 Geometry Optimization and Vibrational Frequency Calculations

To reduce computational cost, initial geometry optimizations were performed in the gas phase using the B3LYP functional [27, 28] with the def2-SVP basis set [32]. We then reoptimized the resulting structures using the wB97X-D functional [31] with the def2-TZVP basis set [32]. This stepwise optimization procedure was adopted primarily to reduce computational cost and to provide robust starting geometries for the higher-level calculations. The gas-phase wB97X-D/def2-TZVP optimized structures were used only as starting geometries for the subsequent solvent-phase

optimizations described below. Although direct solvent optimization is possible, we selected this stepwise procedure for computational efficiency and robust convergence. The four-coordinate geometry around the Cu(II) center was evaluated using the τ_4 index. The τ_4 analysis was performed using the gas-phase wB97X-D/def2-TZVP optimized Cu(II) structures. The τ_4 values were calculated from the two largest coordination angles, α and β (α = N-Cu-N and β = O-Cu-O), according to eq. (1). A τ_4 value of 0 corresponds to an ideal square-planar geometry, whereas a value of 1 corresponds to an ideal tetrahedral geometry [38].

$$\tau_4 = \frac{\{360° - (\alpha + \beta)\}}{141°} \quad (1)$$

To further examine the electronic structure associated with the relatively large coordination-geometry distortion of the Phe complex, natural bond orbital (NBO) analysis was performed for the same gas-phase optimized structure at the wB97X-D/def2-TZVP level.

2.3.2 Excited State Calculations

The gas-phase wB97X-D/def2-TZVP optimized structures were used only as starting geometries and were fully reoptimized in methanol using the wB97X-D functional [31], the def2-TZVP basis set [32], and the SMD implicit solvation model [17]. We performed vibrational frequency calculations at the same level of theory to assess the optimized structures. We then performed excited-state calculations using TD-DFT at the same level of theory in methanol. The simulated UV-vis and CD spectra were generated from the calculated excitation energies, oscillator strengths, and rotatory strengths.

2.3.3 Calculation of Reduction Potentials

We calculated the reduction potential using eq. (2) [19-21];

$$E_{red}\ (vs\ SHE) = -\frac{\Delta G}{nF} - 4.3\ (V) \quad (2)$$

where *n* is the number of electrons, and *F* is the Faraday constant. Δ*G* is the Gibbs free-energy difference between the oxidized and reduced species, as defined in eq. (3).

$$\Delta G = G(Red) - G(Ox) \quad (3)$$

We determined the Gibbs free energies of the oxidized and reduced species using eq. (4).

$$G = E_{elec} + G_{corr} \quad (4)$$

The electronic energy (E_{elec}) was obtained from the "SCF Done" value in single-point energy calculations. At the same time, the thermal correction (G_{corr}) was derived from the "Thermal correction to Gibbs Free Energy" value in vibrational frequency calculations. We used two computational protocols for the reduction-potential calculations. In the B3LYP protocol, the Cu(I), Cu(II), and Cu(III) structures were independently optimized in water using the SMD implicit solvation model [17] at the B3LYP level [27, 28] with 6-31+G(d) for the light elements [29] and LANL2DZ for

Cu [30]. Vibrational frequency calculations and subsequent single-point energy calculations were performed at the same level of theory. In the wB97X-D protocol, the corresponding Cu(I), Cu(II), and Cu(III) structures were independently optimized in SMD water [17] at the wB97X-D/def2-TZVP level [31, 32], followed by vibrational frequency calculations at the same level. To evaluate the final electronic energies with a more flexible basis-set description while limiting the computational cost of geometry optimization and vibrational frequency calculations, single-point energy calculations were performed on the optimized structures at the wB97X-D/def2-TZVPP level [31, 32] using SMD water [17]. For each protocol, the Gibbs free energies were evaluated by combining the single-point electronic energies with the thermal corrections obtained from the corresponding vibrational frequency calculations. We compared the two protocols to assess how the calculated reduction potentials depend on the overall computational protocol. The constant term of -4.3 V was applied to convert the calculated potential to the Standard Hydrogen Electrode (SHE) scale [39].

The HOMO and LUMO energy levels used for comparison with the electrochemical trends were obtained separately from the Cu(II) structures optimized in SMD water [17] at the wB97X-D/def2-TZVP level [31, 32].

2.3.4 Docking Calculation

As a supplementary analysis to examine the influence of the surrounding environment, we performed docking calculations using GOLD software from the Cambridge Crystallographic Data Centre (CCDC) [40]. The crystal structure of laccase from *Trametes versicolor* was obtained from the RCSB Protein Data Bank (PDB ID: 1GYC) and used as the receptor model [41, 42]. The docking search space was defined as a sphere with a radius of 17 Å centered on the Type 1 copper site, considering the size of the Cu(II) complexes. We used the DFT-optimized structures as ligand structures for docking. The top-ranked docking poses were evaluated based on the GOLD score and its component terms.

3. Results and Discussion

3.1 Optimized Structures and Coordination Geometry

Figure 2 shows the optimized structures of the four azo-amino acid Schiff base Cu(II) complexes obtained from DFT calculations. Vibrational frequency analysis found no imaginary frequencies for any DFT-optimized structure, confirming that they correspond to local minima on the potential-energy surface. For the subsequent discussion, the variation in Cu-X bond lengths around the Cu(II) center, the average cis coordination angle, the two trans coordination angles, and the coordination-geometry distortion index, τ_4, were extracted from the optimized structures. Table 1 summarizes these values.

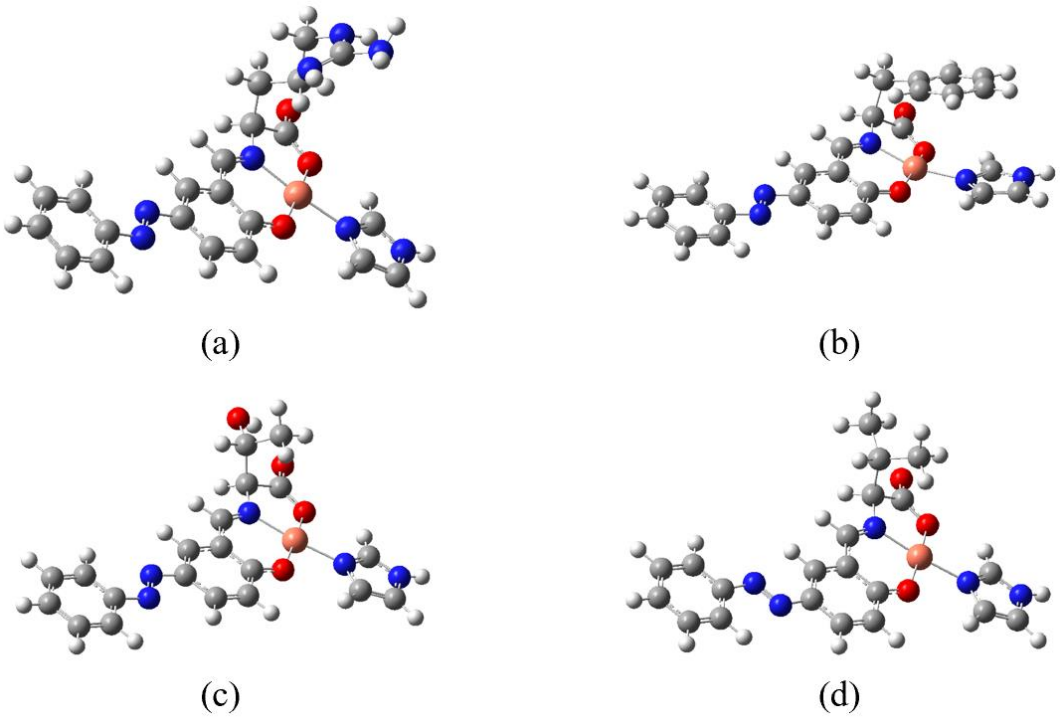

Figure 2 DFT-optimized structures of the azo-amino acid Schiff-base Cu(II) complexes ((a) Arg complex; (b) Phe complex; (c) Thr complex; (d) Val complex).

Table 1 Selected geometric parameters and τ_4 values of DFT-optimized azo-amino acid Schiff base Cu(II) complexes. (Δ(Cu-X) is defined as the difference between the maximum and minimum Cu-X bond lengths, where X represents the four coordinating atoms around the Cu(II) center. The average cis angle was calculated from the four cis X-Cu-X coordination angles around the Cu(II) center, excluding the two trans angles. τ_4 was calculated from the two largest coordination angles.

complex	Δ(Cu-X)/Å	average cis angle/°	trans (O-Cu-O)/°	trans (N-Cu-N)/°	τ_4
Arg	0.080	90.03	176.25	174.44	0.066
Phe	0.061	90.79	167.10	164.13	0.204
Thr	0.078	90.04	175.90	174.18	0.070
Val	0.078	90.05	175.15	174.10	0.076

There were no large differences in Δ(Cu-X) among the optimized structures of the four complexes. The Δ(Cu-X) values were 0.061 to 0.080 Å, indicating that the amino acid-derived substituents had only a limited effect on the Cu-ligand bond-length variation within the primary coordination sphere. The average cis angles were also close to 90° for all complexes, suggesting that the local coordination environment around Cu(II) was approximately square planar. In contrast, the trans coordination angles showed more pronounced differences, especially in the Phe complex. The Arg, Thr, and Val complexes showed trans O-Cu-O and N-Cu-N angles close to 180°, whereas the corresponding angles in the Phe complex decreased to 167.10° and 164.13°, respectively. Furthermore, when using the tetrahedral geometric parameter τ_4 to quantify differences in coordination geometry, the Arg, Thr, and Val complexes showed values of approximately 0.07 to 0.08. A τ_4 value closer to zero indicates greater square-planar character. The Phe complex showed

a significantly higher value of approximately 0.204. This indicates that the Phe complex exhibited the greatest deviation from an ideal square-planar geometry among the four complexes. The larger τ_4 value of the Phe complex therefore arises primarily from angular distortion of the coordination environment rather than from unusually large variations in the Cu-ligand bond lengths. As an experimental reference for comparison, the crystal structure of a closely related L-leucine-derived azo-amino acid Schiff-base Cu(II) complex with an imidazole ligand [35] exhibits an approximately square-planar Cu(II) coordination environment. The two independent molecules in the crystal structure show trans N-Cu-N angles of 175.37° and 174.23° and trans O-Cu-O angles of 177.38° and 177.84°, respectively, corresponding to estimated τ_4 values of 0.051 and 0.056. These experimentally derived values are similar to the calculated τ_4 values of the Arg, Thr, and Val complexes (0.066-0.076), whereas the Phe complex shows a substantially larger value of 0.204. To further examine the electronic structure associated with this distortion, we performed NBO analysis using the same gas-phase optimized structure of the Phe complex. Natural population analysis yielded a natural charge of +1.04e on the Cu center, while the natural electron configuration showed a Cu 3d population of approximately 9.29 electrons. These results indicate appreciable electronic interaction between the Cu center and the coordinating ligand atoms. Although this present analysis does not allow the distortion to be assigned uniquely to a specific steric, π-π, or other noncovalent interaction, the combined geometric and NBO results suggest that the enhanced distortion of the Phe complex reflects coupled conformational and electronic effects.

3.2 UV-vis and CD Spectra

Figure 3 and Figure 4 show the experimental and calculated UV-vis and CD spectra, respectively, for each complex. Table 2 and Table 3 summarize quantitative comparisons of the selected near-UV absorption and CD features, respectively.

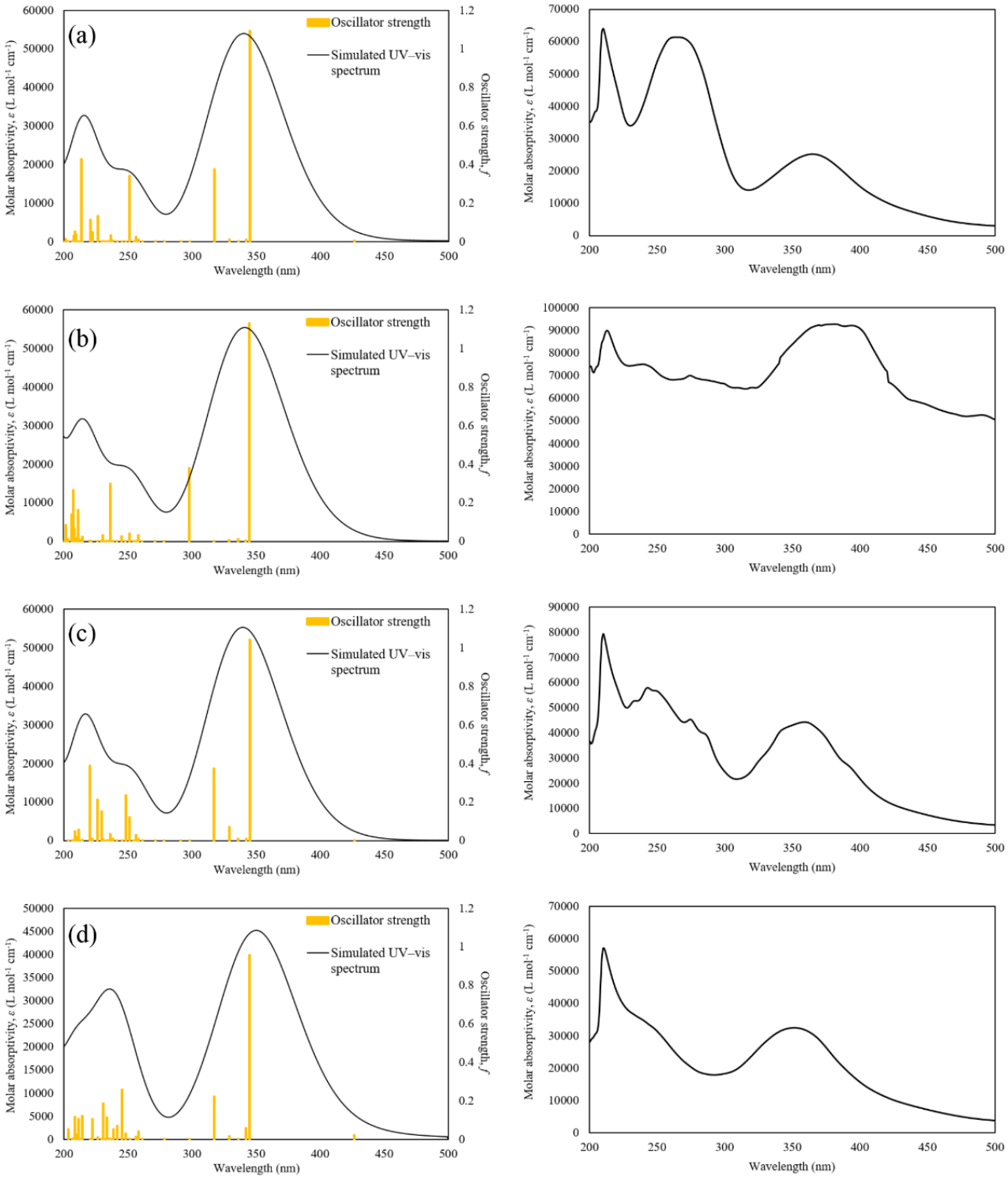

Figure 3 UV-vis spectra of azo-amino acid Schiff base Cu(II) complexes (left: calculated values, right: experimental values. (The legend in the upper right indicates the concentration of the sample solution.) (a) Arg complex; (b) Phe complex; (c) Thr complex; (d) Val complex.

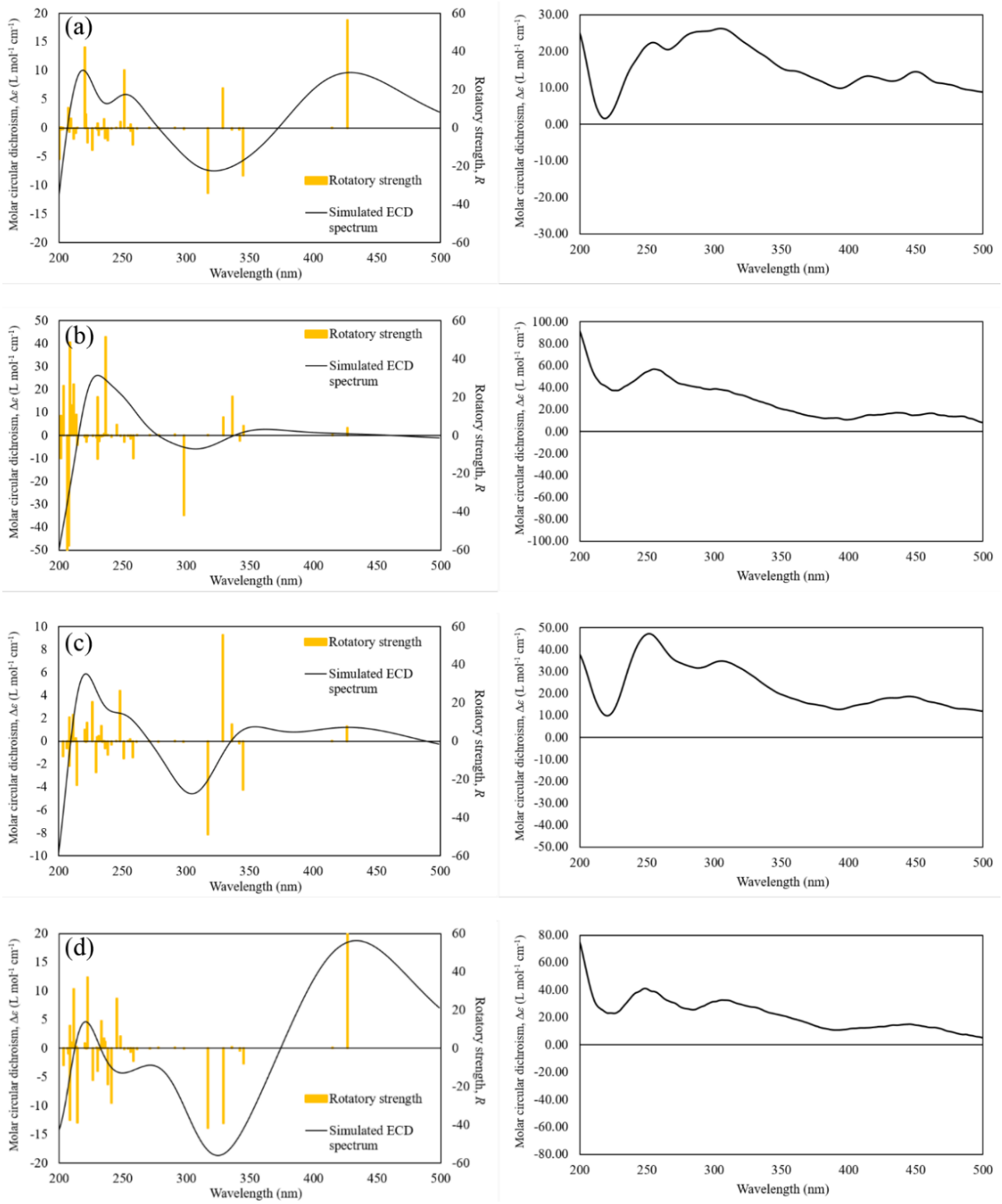

Figure 4 CD spectra of azo-amino acid Schiff base Cu(II) complexes (left: calculated values, right: experimental values. (The legend in the upper right indicates the concentration of the sample solution.) (a) Arg complex; (b) Phe complex; (c) Thr complex; (d) Val complex.

Table 2 Selected experimental and calculated near-UV absorption parameters of azo-amino acid Schiff base Cu(II) complexes. (λ_{exp} represents the experimental absorption feature, λ_{calc} represents the calculated excitation wavelength, and $|\Delta\lambda|$ is defined as $|\lambda_{calc} - \lambda_{exp}|$. f denotes the oscillator strength. Percentages for the dominant MO transitions represent approximate configurational contributions estimated from the squared excitation coefficients. α and β denote alpha- and beta-spin molecular orbitals, respectively. LC denotes ligand-centered. For the Phe complex, the experimental near-UV spectrum showed a broad absorption plateau between 361 and 401 nm; therefore, the experimental feature is reported as a wavelength range and $|\Delta\lambda|$ was not calculated.

Complex	λ_{exp}/nm	λ_{calc}/nm	$\lvert\Delta\lambda\rvert$/nm	*f*	Dominant MO transitions (%)	Electronic assignment
Arg	364	345.99	18.01	1.0931	133α → 134α (43.6) 132β → 133β (45.3)	LC π → π*
Phe	361-401 (broad)	347.13	-	1.1309	130α → 131α (44.1) 129β → 130β (45.5)	LC π → π*
Thr	359	345.92	13.08	1.0420	118α → 119α (43.2) 117β → 118β (44.3)	LC π → π*
Val	351	353.90	2.90	0.9586	118α → 119α (37.4) 117β → 118β (42.8)	LC π → π*

Table 3 Selected experimental and calculated CD features of the azo-amino acid Schiff-base Cu(II) complexes. λ_{exp} and $\Delta\varepsilon_{exp}$ denote the experimental values, whereas λ_{calc} and $\Delta\varepsilon_{calc}$ refer to extrema of the broadened simulated ECD spectra. $|\Delta\lambda|$ is defined as $|\lambda_{calc} - \lambda_{exp}|$. "TD-DFT excitation(s)" denotes the wavelength(s) of the individual vertical excitation(s) that principally contribute to each broadened calculated ECD feature. The listed R(length) values correspond to these individual excitations. R(length) represents the rotatory strength of an individual vertical excitation and is therefore not directly equivalent to Δε obtained from the broadened simulated ECD spectrum. "Positive" indicates a positive experimental CD feature when a single representative Δε value was not assigned.

complex	λ_{exp}/nm	$\Delta\varepsilon_{exp}$	λ_{calc}/nm	$\Delta\varepsilon_{calc}$	$\|\Delta\lambda\|$/nm	TD-DFT excitation (s)/nm	R (length)
Arg	255	+22.30	252	+5.8343	3	251.96	+30.2614
	305	+26.16	322	-7.5156	17	317.36	-34.1454
						329.97	+20.8150
	415-450	positive	429	+9.6582	-	427.22	+56.5125
Phe	255	+56.84	230	+26.2791	25	251.19	+51.4163
						220.62	+48.7745
						216.34	+45.1594
						226.07	+26.5952
	300-320	positive	307	-5.8625	-	317.69	-41.7512
	350-370	positive	362	+2.6716	-	337.03	+20.2482
						335.31	+9.5159
						347.13	+4.9843
Thr	252	+47.32	222	+5.8521	30	220.95	+20.4446
						220.05	+9.5678
						226.27	-16.2413
	305-306	+34.85	305	-4.5977	0-1	318.57	-48.8895
	445	+18.70	428	+1.1928	17	428.43	+7.5604
Val	249	+41.24	250	-4.3068	1	244.34	-28.6578
						243.73	-18.7076
						246.60	+25.8928
	306	+32.77	325	-18.6774	19	316.53	-41.5701
						331.59	-39.1773
	445	+15.13	434	+18.7381	11	432.90	+109.6746

Regarding the UV-vis spectra, the higher-energy absorption region below approximately 270 nm contains several closely spaced calculated excitations and was therefore not assigned to a single TD-DFT state. To clarify the electronic origins of the intense near-UV absorption bands, we examined the dominant TD-DFT excitation components and the spatial distributions of the corresponding molecular orbitals (Table 2). The intense calculated transitions were obtained at 345.99 nm for Arg (f = 1.0931), 347.13 nm for Phe (f = 1.1309), 345.92 nm for Thr (f = 1.0420), and 353.90 nm for Val

(f = 0.9586). In each complex, the excitation is dominated by paired α- and β-spin molecular-orbital transitions, with their approximate configurational contributions summarized in Table 2. Inspection of the corresponding occupied and virtual molecular orbitals showed that they are predominantly distributed over the conjugated azo-Schiff-base ligand framework. These intense near-UV bands are therefore assigned mainly to ligand-centered π → π* excitations rather than to predominantly metal-to-ligand or ligand-to-metal charge-transfer transitions. Minor mixing with orbitals influenced by the Cu coordination environment cannot be excluded; however, no predominant MLCT or LMCT character was identified for these intense transitions. The quantitative comparison of selected experimental and calculated CD features is summarized in Table 3. In the approximately 300-325 nm region, the experimental CD features are positive for all four complexes. In contrast, the calculated spectra show negative features at 322, 307, 305, and 325 nm for the Arg, Phe, Thr, and Val complexes, respectively. In particular, the calculated negative feature of the Thr complex at 305 nm nearly coincides with the experimental positive feature at 305-306 nm. In comparison, the calculated Val feature at 250 nm differs by only 1 nm from the experimental positive feature at 249 nm but has the opposite sign. These results show that close agreement in wavelength does not necessarily indicate correct reproduction of the CD sign. At longer wavelengths, the calculated positive features at 429, 428, and 434 nm for the Arg, Thr, and Val complexes, respectively, reproduce the experimentally observed positive sign. For the Phe complex, the calculated positive feature at 362 nm lies within the experimental positive region at approximately 350-370 nm. The wavelength, sign, and intensity discrepancies in the CD spectra highlight several sources of uncertainty in the present computational treatment. We performed the calculations at the wB97X-D/def2-TZVP level with the SMD solvation model using a single optimized conformer, without vibronic effects or conformational averaging. In addition, the continuum solvation model does not explicitly represent specific solvent orientations, hydrogen bonding, or other local solvent-complex interactions. Therefore, the remaining discrepancies may reflect the combined effects of the choice of functional and basis set, TD-DFT limitations for excited states with appreciable charge-transfer character, conformational variability, vibronic effects, and the approximate treatment of solvation. Because these factors were not examined independently, their relative contributions cannot be determined from the present results. The variation in the degree of agreement among the different spectral regions and complexes further suggests that complex-specific electronic-structure and conformational effects may also contribute. Comparative calculations using alternative computational levels, multiple conformers, and microsolvated models could help distinguish these effects.

3.3 Electrochemical Properties

3.3.1 CV

Figure 5 shows the CVs of the four complexes.

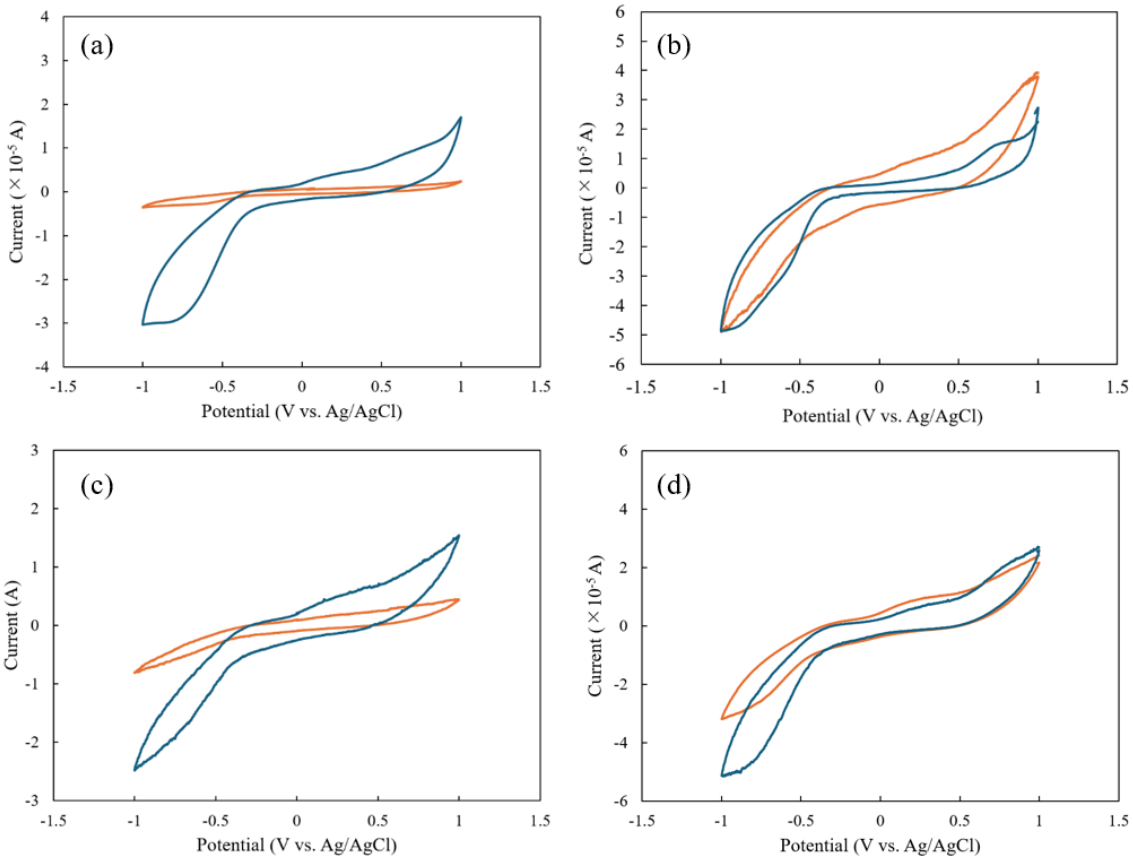

Figure 5 CV of azo-amino acid Schiff base Cu(II) complexes ((a) Arg complex; (b) Phe complex; (c) Thr complex; (d) Val complex, under N_2 atmosphere (orange) and O_2 atmosphere (blue)).

Although no sharp and well-defined redox peaks were observed, a gradual increase in cathodic current became apparent from approximately -0.3 V vs Ag/AgCl. In addition, a broad reduction feature was observed at approximately -0.7 to -0.8 V vs Ag/AgCl. Because the cathodic responses were broad and irreversible, a unique equilibrium reduction potential could not be determined for each complex from the present CV data. The observed irreversibility may partly reflect structural reorganization coupled to electron transfer. Comparison of the DFT-optimized Cu(II) and Cu(I) structures indicated oxidation-state-dependent relaxation of the Cu-ligand coordination environment. Such structural relaxation may contribute to the broad irreversible reduction responses. However, the present data cannot distinguish these present data possible contributions from subsequent chemical reactions or electrode adsorption.

3.3.2 Reduction Potential Prediction

Table 4 shows the standard reduction potentials for Cu(II)/Cu(I) and Cu(III)/Cu(II) couples of each complex predicted from DFT calculations.

Table 4 Calculated reduction potentials (V vs SHE) of azo-amino acid Schiff base Cu(II) complexes.

	Arg		Phe		Thr		Val	
	Cu(II)/Cu(I)	Cu(III)/Cu(II)	Cu(II)/Cu(I)	Cu(III)/Cu(II)	Cu(II)/Cu(I)	Cu(III)/Cu(II)	Cu(II)/Cu(I)	Cu(III)/Cu(II)
E_{red} (V vs SHE) (B3LYP/6-31+G(d), LANL2DZ)	-0.515	1.021	-0.492	1.014	-0.428	1.074	-0.471	1.002
E_{red} (V vs SHE) (wB97X-D/def2-TZVPP)	-0.724	1.099	-0.782	1.090	-0.727	1.119	-0.795	1.066
ΔE_{red} (V vs SHE) (wB97X-D-B3LYP)	-0.209	0.078	-0.290	0.076	-0.299	0.045	-0.324	0.064

The predicted reduction potential varied significantly between the two computational protocols. The largest difference was observed for the standard reduction potential of the Val Cu(II)/Cu(I) couple, with a discrepancy of 0.324 V. Furthermore, regarding the Cu(II)/Cu(I) potential, the B3LYP-based protocol predicted the highest potential for the Thr complex. In contrast, the wB97X-D-based protocol predicted the most positive potential for the Arg complex. These results show that both the calculated values and the relative ordering of the complexes depend on the overall computational protocol. Thus, the present calculations clearly show that the predicted Cu(II)/Cu(I) reduction potentials are substantially dependent on the overall computational protocol. However, because the functional and basis-set treatments changed simultaneously between the two protocols, we cannot separate their individual contributions to these differences. The broad experimental reduction feature observed at approximately -0.7 to -0.8 V vs Ag/AgCl corresponds to approximately -0.5 to -0.6 V vs SHE. The potential range of the broad irreversible reduction feature was closer to the calculated Cu(II)/Cu(I) potentials than to the Cu(III)/Cu(II) potentials, providing a tentative basis for assignment to the Cu(II)/Cu(I) process. However, because the experimentally observed response was broad and irreversible, whereas the calculated values represent thermodynamic reduction potentials, the experimental response may also include contributions from structural reorganization and kinetic processes following electron transfer. Therefore, this comparison should be regarded as qualitative rather than quantitative. The B3LYP-based Cu(II)/Cu(I) potentials (-0.515 to -0.428 V vs SHE) were numerically closer to the experimentally observed broad reduction region (approximately -0.5 to -0.6 V vs SHE) than the wB97X-D/def2-TZVPP values (-0.795 to -0.724 V vs SHE). However, because the experimental cathodic responses were broad and irreversible, we could not extract well-defined equilibrium reduction potentials for the individual complexes. Accordingly, formal absolute deviations (|ΔE|) and mean absolute errors (MAEs) relative to experimental thermodynamic reduction potentials were not calculated, because assigning a single experimental potential for each complex would require an arbitrary operational definition and would imply an unjustified equivalence between the irreversible CV response and the calculated thermodynamic reduction potential. The closer numerical agreement of the B3LYP-based values should therefore not be interpreted as demonstrating that this protocol is intrinsically more accurate, because kinetic effects, oxidation-state-dependent structural reorganization, and possible error cancellation may contribute to the apparent agreement. Predicting reduction potentials from ΔG is theoretically sound because it incorporates oxidation-state-dependent structural relaxation, thermal corrections, and solvation. However, the remaining discrepancies between the calculated and experimental electrochemical behavior also suggest a limitation of the present implicit-solvent treatment. Although the SMD model accounts for the bulk dielectric response of water, it does not explicitly describe local solute-solvent interactions around the metal center. In particular, first-shell water molecules may interact differently with the Cu(II) and Cu(I) states through hydrogen bonding, electrostatic interactions, or transient coordination, potentially affecting both structural reorganization and reduction free energies.

3.3.3 HOMO-LUMO

Figure 6 shows the calculated HOMO and LUMO energy levels and the corresponding HOMO-LUMO gaps.

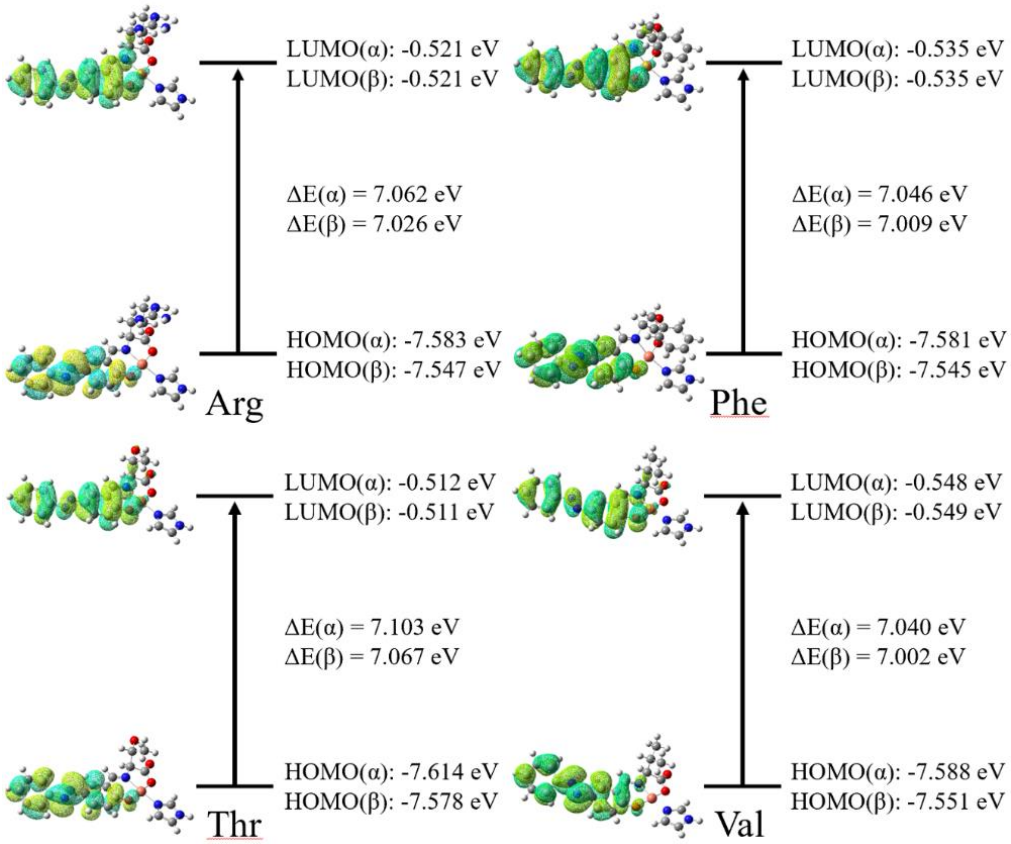

Figure 6 Frontier orbital levels of azo-amino acid Schiff base Cu(II) complexes.

The HOMO-LUMO gaps showed little variation among the four complexes, indicating that the amino acid-derived substituents had only a small effect on the overall frontier orbital energy gap. In contrast, the LUMO energy levels followed the order Thr > Arg > Phe > Val. In related Cu(II) complexes, lower LUMO energy levels have been correlated with greater reducibility [9]. Based on the frontier-orbital calculations in this study, the Val complex would therefore be expected to be the most readily reduced.

However, this ordering did not match that obtained from the ΔG-based reduction-potential calculations described above. This discrepancy reflects the different physical meanings of the two descriptors: the LUMO energy is an orbital-based descriptor of the electronic structure of a single oxidation state, whereas the reduction potential derived from ΔG reflects the free-energy difference between the independently relaxed Cu(II) and Cu(I) states, including oxidation-state-dependent structural reorganization, thermal corrections, and solvation effects. Furthermore, the ΔG-based reduction potentials themselves showed substantial dependence on the computational protocol, with differences of 0.21-0.32 V between the B3LYP and wB97X-D protocols and changes in the predicted ordering of reducibility. Because identifying the specific electronic origin of this divergence would require a systematic analysis of both oxidation states across the full series, we limit our interpretation to the trends supported by the present calculations and do not assign the discrepancy to a specific electronic redistribution mechanism. These results highlight a key limitation of using either frontier-orbital energies or reduction potentials from a single computational protocol as quantitative predictors of redox behavior in transition-metal complexes.

Benchmarking against well-defined reversible experimental redox potentials under matched conditions would help access the magnitude of these method-dependent errors.

3.4 Docking Calculation

Figure 7 shows the top-ranked docking poses near the Type 1 copper site obtained using GOLD. The displayed structures include residues located within 4 Å of each complex. Table 5 summarizes the GOLD scores and their component terms for the four complexes.

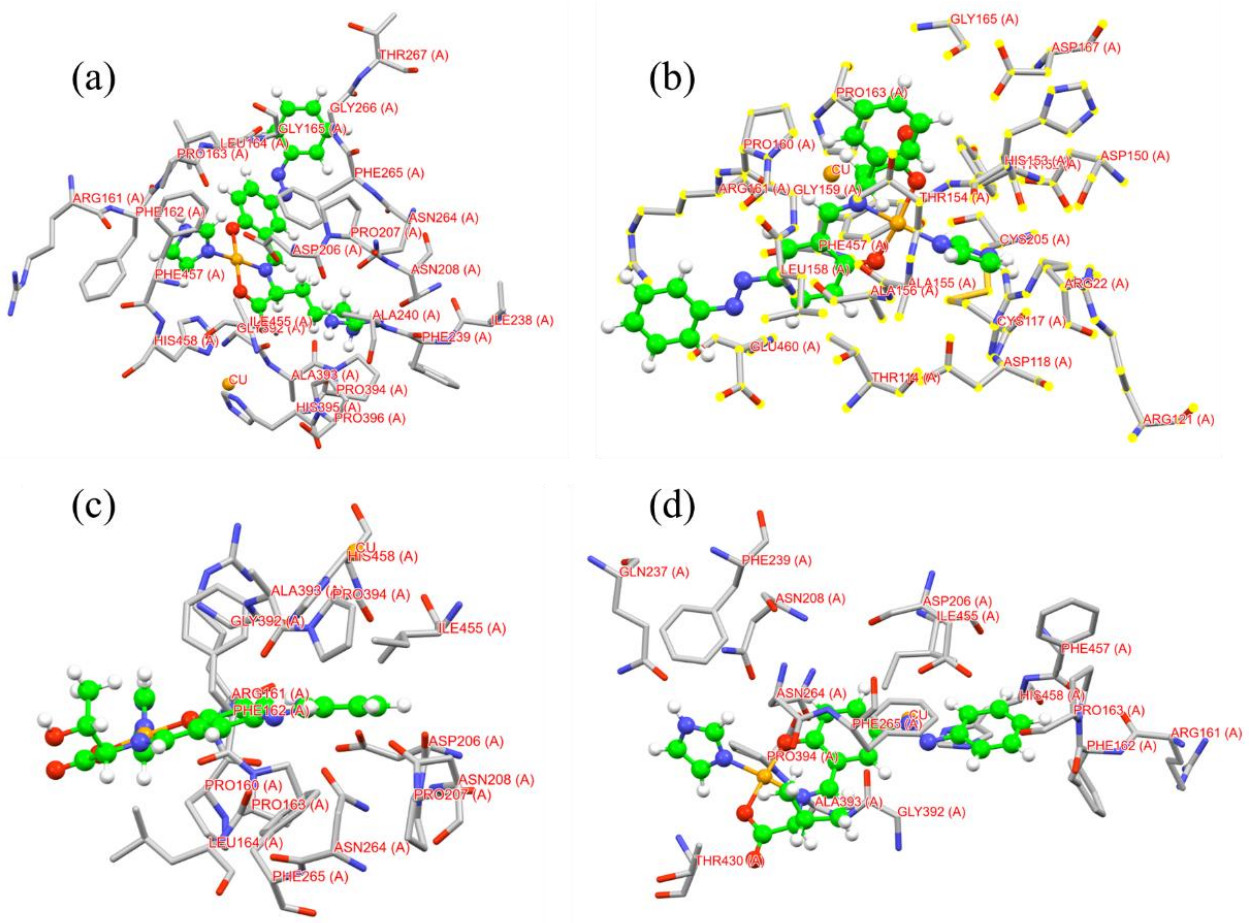

Figure 7 Docking poses (within 4 Å) of the azo-amino acid Schiff-base Cu(II) complexes ((a) Arg complex; (b) Phe complex; (c) Thr complex; (d) Val complex).

Table 5 GOLD scores and component terms for each complex.

	Arg	Phe	Thr	Val
Goldscore.Fitness	59.9079	56.9975	45.5997	50.4599
Goldscore.External.HBond.Weighted	3.3783	0.0000	0.0000	1.1847
Goldscore.External.Vdw.Weighted	62.7890	61.1318	48.3464	51.6683
Goldscore.Internal.Torsion.Weighted	-5.4080	-1.1367	-1.0814	-1.6697
Goldscore.Internal.Vdw.Weighted	-0.3608	1.0869	-2.8007	-0.7946

The GOLD score analysis showed that the “External Vdw” term made the largest contribution for all complexes, suggesting that hydrophobic interactions in the cavity near the Type 1 copper site dominate during docking. For the Arg and Val complexes, the “External Hbond” term also made a small favorable contribution, suggesting the presence of local polar interactions. Furthermore, docking poses within 4 Å showed many hydrophobic residues (e.g., Ala, Gly, Pro) and aromatic residues (e.g., Phe, His) within 4 Å of the complexes. These results are consistent with docking within a hydrophobic pocket near the Type 1 copper site.

4. Conclusions

In this study, we assessed the reliability and limitations of DFT and TD-DFT calculations for predicting the spectroscopic and electrochemical properties of four azo-amino acid Schiff-base Cu(II) complexes. The optimized coordination geometries were generally close to square planar, whereas the phenylalanine complex exhibited the largest distortion, with a τ_4 value of 0.204. TD-DFT qualitatively reproduced some major features of the experimental UV-vis and CD spectra; however, the calculated UV-vis bands were generally shifted toward shorter wavelengths, whereas the CD spectra showed discrepancies in wavelength, intensity, and sign. Most notably, the positive experimental CD features in the approximately 300-325 nm region were predicted with the opposite sign for all four complexes, showing that agreement in peak position alone does not ensure correct reproduction of the chiroptical response. However, some longer-wavelength positive CD features were reproduced with the correct sign. These discrepancies should not be attributed solely to the SMD implicit solvation model. They may arise from the combined effects of the choice of functional and basis set, TD-DFT limitations for excited states with appreciable charge-transfer character, the neglect of vibronic effects and conformational averaging, and the incomplete description of specific solvent-complex interactions.

For the Cu(II)/Cu(I) couples, the calculated reduction potentials differed by 0.21-0.32 V between the two computational protocols, and the predicted ordering of reducibility also changed between the two protocols. These results demonstrate substantial computational-protocol dependence of both the calculated reduction potentials and the relative ordering of the complexes. Because the functional and basis-set treatments changed simultaneously between the two protocols, however, we can not seperate individual contributions to these differences from the present calculations. Furthermore, this ordering was inconsistent with the trend inferred from the LUMO energies. This inconsistency represents a central finding of this study: qualitative agreement in spectral profiles or frontier-orbital trends does not necessarily ensure quantitatively reliable predictions of the redox behavior of transition-metal complexes. Unlike the LUMO energy, which is an orbital-based descriptor of a single oxidation state, a ΔG-based reduction potential includes oxidation-state-dependent structural relaxation, thermal corrections, and solvation. Together with the spectroscopic discrepancies described above, these results emphasize the need for property-specific benchmarking and careful evaluation of the computational protocol and environmental treatment when applying DFT and TD-DFT to transition-metal complexes in solution.

The docking results further illustrated that the complexes may experience different local molecular environments near the Type 1 copper site of laccase. However, interpret the resulting docking poses as qualitative models of possible environmental effects rather than as direct evidence of an electron-transfer mechanism. Future work should progressively extend the present implicit-

solvent treatment by introducing explicit first-shell solvent molecules in microsolvation models, followed by cluster-continuum and environmental-embedding approaches. Because both spectroscopic and redox properties may depend on molecular conformation and local solvent arrangement, these approaches should ideally be combined with conformational and solvent-configuration sampling. Such developments would help distinguish limitations arising from the electronic-structure method from those associated with the continuum treatment of solvation. They would provide a route toward a more realistic description of local-environment-dependent spectroscopic responses and redox behavior, including specific solvent orientations, hydrogen bonding, and transient solvent coordination around the metal center.

Acknowledgments

The computation was performed using Research Center for Computational Science, Okazaki, Japan (Project: 25-IMS-C169 and 26-IMS-C179).

Author Contributions

Experiments (S. I.), calculations (A. H., M. N.), data analysis (A. H.), preparation of figures and tables (A. H., M. N.), writing the manuscript (A. H.), contributing to the writing of the Introduction (S. H.), revising the manuscript (M. N., D. N., S. H., T. A.), supervision (T. A.).

Funding

This work was supported by a Grant-in-Aid for Scientific Research (B) KAKENHI (Grant Number: 24K00912) from the Japan Society for the Promotion of Science (JSPS).

Competing Interests

The authors have declared that no competing interests exist.

Data Availability Statement

All data generated or analyzed during this study are included in this published article.

AI-Assisted Technologies Statement

During the preparation of this manuscript, the authors used ChatGPT, developed by OpenAI, solely for English translation, grammatical checking, and refinement of word choice and expression. ChatGPT was not used for data generation or analysis, figure or table preparation, or the creation of the scientific content of the manuscript. The authors reviewed and verified all AI-assisted revisions and take full responsibility for the final content of the manuscript.

References

1. Jacob CR, Neugebauer J. Subsystem density-functional theory (update). Wiley Interdiscip Rev Comput Mol Sci. 2024; 14: e1700.

2. Cardot C. Density functional theory augmented multiplet ligand field theory applied to X-ray spectroscopy of 3d transition metals. Seattle, WA: University of Washington; 2025.
3. Amrutkar RD, Indaji PS, Chaudhari DB, Waghmode NA, Jadhav MA. Advancements in TD-DFT: A comprehensive review. Curr Drug Res Rev. 2025. doi: 10.2174/0125899775385222251001062232.
4. Liao MS, Huang MJ, Watts JD. Effects of local protein environment on the binding of diatomic molecules to heme in myoglobins. DFT and dispersion-corrected DFT studies. J Mol Model. 2013; 19: 3307-3323.
5. Cramer CJ, Truhlar DG. Density functional theory for transition metals and transition metal chemistry. Phys Chem Chem Phys. 2009; 11: 10757-10816.
6. Neese F. Prediction of molecular properties and molecular spectroscopy with density functional theory: From fundamental theory to exchange-coupling. Coord Chem Rev. 2009; 253: 526-563.
7. Cohen AJ, Mori-Sánchez P, Yang W. Insights into current limitations of density functional theory. Science. 2008; 321: 792-794.
8. Perdew JP, Zunger A. Self-interaction correction to density-functional approximations for many-electron systems. Phys Rev B. 1981; 23: 5048.
9. Conradie MM, Langner EHG, Conradie J. DFT data to relate calculated LUMO energy with experimental reduction potentials of Cu(II)-β-diketonato complexes. Data Brief. 2021; 38: 107331.
10. Perdew JP, Parr RG, Levy M, Balduz JL. Density-functional theory for fractional particle number: Derivative discontinuities of the energy. Phys Rev Lett. 1982; 49: 1691.
11. Dreuw A, Head-Gordon M. Failure of time-dependent density functional theory for long-range charge-transfer excited states. J Am Chem Soc. 2004; 126: 4007-4016.
12. Marques MAL, Gross EKU. Time-dependent density functional theory. Annu Rev Phys Chem. 2004; 55: 427-455.
13. Autschbach J. Time-dependent density functional response theory for electronic chiroptical properties of chiral molecules. Top Curr Chem. 2011; 298: 1-98.
14. Tomasi J, Mennucci B, Cammi R. Quantum mechanical continuum solvation models. Chem Rev. 2005; 105: 2999-3094.
15. Cossi M, Rega N, Scalmani G, Barone V. Energies, structures, and electronic properties of molecules in solution with the C-PCM solvation model. J Comput Chem. 2003; 24: 669-681.
16. Klamt A, Schüürmann G. COSMO: A new approach to dielectric screening in solvents with explicit expressions for the screening energy and its gradient. J Chem Soc Perkin Trans 2. 1993; 22: 799-805.
17. Marenich AV, Cramer CJ, Truhlar DG. Universal solvation model based on solute electron density and on a continuum model of the solvent defined by the bulk dielectric constant and atomic surface tensions. J Phys Chem B. 2009; 113: 6378-6396.
18. Boereboom JM, Fleurat-Lessard P, Bulo RE. Explicit solvation matters: Performance of QM/MM solvation models in nucleophilic addition. J Chem Theory Comput. 2018; 14: 1841-1852.
19. Baik MH, Friesner RA. Computing redox potentials in solution: Density functional theory as a tool for rational design of redox agents. J Phys Chem A. 2002; 106: 7407-7412.
20. Winget P, Cramer CJ, Truhlar DG. Computation of equilibrium oxidation and reduction potentials for reversible and dissociative electron-transfer reactions in solution. Theor Chem Acc. 2004; 112: 217-227.

21. Marenich AV, Ho J, Coote ML, Cramer CJ, Truhlar DG. Computational electrochemistry: Prediction of liquid-phase reduction potentials. Phys Chem Chem Phys. 2014; 16: 15068-15106.
22. Trasatti S. The absolute electrode potential: An explanatory note (Recommendations 1986). Pure Appl Chem. 1986; 58: 955-966.
23. Behzad M, Ghasemi L, Mehraban F, Abbasi A, Ashfaq M, Arab A. Structural elucidation, DFT and Hirshfeld surface analysis, and molecular docking studies of N_2O_2-type Schiff base ligands and their Cu(II) and Ni(II) complexes targeting COVID-19 and its omicron variant main proteases. Inorg Chem Commun. 2025; 182: 115465.
24. Kargar H, Abyar F, Fallah-Mehrjardi M, Acar E, Dege N, Ashfaq M, et al. Synthesis, SC-XRD, HSA, DFT calculations, and molecular docking studies of a new Cu(I) complex bearing the bidentate Schiff base derived from trimethylenediamine and 4-cyanobenzaldehyde. Phys Chem Res. 2026; 14: 9-27.
25. Abd El-Hamid SM, Aziz SW, Sadeek SA, Sabry MA, El-Gedamy MS. Synthesis, spectral analysis, XRD, molecular docking simulation of dithranol and glycine mixed ligand complexes and their potential role in suppressing breast cancer cells via down-regulating the expression of protein metalloproteinase-9. Appl Organomet Chem. 2024; 38: e7650.
26. Hassan AU, Sumrra SH, Mustafa G, Zubair M, Mohyuddin A, Nkungli NK, et al. Molecular modeling of mordant black dye for future applications as visible light harvesting materials with anchors: Design and excited state dynamics. J Mol Model. 2023; 29: 74.
27. Becke AD. Density-functional thermochemistry. III. The role of exact exchange. J Chem Phys. 1993; 98: 5648-5652.
28. Lee C, Yang W, Parr RG. Development of the Colle-Salvetti correlation-energy formula into a functional of the electron density. Phys Rev B. 1988; 37: 785.
29. Hariharan PC, Pople JA. The influence of polarization functions on molecular orbital hydrogenation energies. Theor Chim Acta. 1973; 28: 213-222.
30. Hay PJ, Wadt WR. Ab initio effective core potentials for molecular calculations. Potentials for the transition metal atoms Sc to Hg. J Chem Phys. 1985; 82: 270-283.
31. Chai JD, Head-Gordon M. Systematic optimization of long-range corrected hybrid density functionals. J Chem Phys. 2008; 128: 084106.
32. Weigend F, Ahlrichs R. Balanced basis sets of split valence, triple zeta valence and quadruple zeta valence quality for H to Rn: Design and assessment of accuracy. Phys Chem Chem Phys. 2005; 7: 3297-3305.
33. Singha A, Sekretareva A, Tao L, Lim H, Ha Y, Braun A, et al. Tuning the type 1 reduction potential of multicopper oxidases: Uncoupling the effects of electrostatics and H-bonding to histidine ligands. J Am Chem Soc. 2023; 145: 13284-13301.
34. Kashiwagi K, Tassinari F, Haraguchi T, Banerjee-Gosh K, Akitsu T, Naaman R. Electron transfer via helical oligopeptide to laccase including chiral Schiff base copper mediators. Symmetry. 2020; 12: 808.
35. Kaneda A, Suzuki S, Nakane D, Kashiwagi Y, Akitsu T. Crystal structure and Hirshfeld surface analysis of (1*H*-imidazole-κN^3) [4-methyl-2-({[2-oxido-5-(2-phenyldiazen-1-yl)phenyl]methylidene}amino)pentanoate-κ^{3}O,*N,O*′]copper(II). Acta Crystallogr E Crystallogr Commun. 2024; 80: 468-471.

36. Narita M, Yamamoto Y, Nakane D, Akitsu T, Pinlap BR, Kamdem BP, et al. Correlation between calculated electronic properties and antibacterial activity of chiral amino acid Schiff base copper(II) complexes. Discov Chem. 2025; 2: 185.
37. Frisch MJ, Trucks GW, Schlegel HB, Scuseria GE, Robb MA, Cheeseman JR, et al. Gaussian 09, Revision E.01. Wallingford, CT: Gaussian, Inc.; 2013.
38. Yang L, Powell DR, Houser RP. Structural variation in copper(I) complexes with pyridylmethylamide ligands: Structural analysis with a new four-coordinate geometry index, τ_4. Dalton Trans. 2007; 36: 955-964.
39. Harb H, Assary RS. Systematic improvement of redox potential calculation of Fe(III)/Fe(II) complexes using a three-layer micro-solvation model. Phys Chem Chem Phys. 2025; 27: 10717-10729.
40. Jones G, Willett P, Glen RC, Leach AR, Taylor R. Development and validation of a genetic algorithm for flexible docking. J Mol Biol. 1997; 267: 727-748.
41. Choinowski T, Antorini M, Piontek K. Crystal structure determination at room temperature of a laccase from *Trametes versicolor* in its oxidised form containing a full complement of copper ions [Internet]. 2024. Available from: https://www.wwpdb.org/pdb?id=pdb_00001gyc.
42. Piontek K, Antorini M, Choinowski T. Crystal structure of a laccase from the fungus *Trametes versicolor* at 1.90 Å resolution containing a full complement of coppers. J Biol Chem. 2002; 277: 37663-37669.